

Band-Order Anomaly at the γ -Al₂O₃/SrTiO₃ Interface Drives the Electron-Mobility Boost

Alla Chikina,¹ Dennis V. Christensen,² Vladislav Borisov,³ Marius-Adrian Husanu,^{1,4} Yunzhong Chen,² Xiaoqiang Wang,¹ Thorsten Schmitt,¹ Milan Radovic,¹ Naoto Nagaosa,⁵ Andrey S. Mishchenko,⁵ Roser Valentí,³ Nini Pryds² & Vladimir N. Strocov¹

¹*Swiss Light Source, Paul Scherrer Institute, 5232 Villigen-PSI, Switzerland*

²*Department of Energy Conversion and Storage, Technical University of Denmark, 2800 Kgs. Lyngby, Denmark*

³*Institut für Theoretische Physik, Goethe-Universität Frankfurt am Main, 60438 Frankfurt am Main, Max-von-Laue-Strasse 1, Germany*

⁴*National Institute of Materials Physics, Atomistilor 405A, 077125 Magurele, Romania*

⁵*RIKEN Center for Emergent Matter Science, 2-1 Hirosawa, Wako, Saitama 351-0198, Japan*

Abstract

Rich functionalities of transition-metal oxides and their interfaces bear an enormous technological potential. Its realization in practical devices requires, however, a significant improvement of yet relatively low electron mobility in oxide materials. Recently, a mobility boost of about two orders of magnitude has been demonstrated at the spinel/perovskite $\gamma\text{-Al}_2\text{O}_3/\text{SrTiO}_3$ interface compared to the paradigm perovskite/perovskite $\text{LaAlO}_3/\text{SrTiO}_3$. We explore the fundamental physics behind this phenomenon from direct measurements of the momentum-resolved electronic structure of this interface using resonant soft-X-ray angle-resolved photoemission. We find an anomaly in orbital ordering of the mobile electrons in $\gamma\text{-Al}_2\text{O}_3/\text{SrTiO}_3$ which depopulates electron states in the top STO layer. This rearrangement of the mobile electron system pushes the electron density away from the interface that reduces its overlap with the interfacial defects and weakens the electron-phonon interaction, both effects contributing to the mobility boost. A crystal-field analysis shows that the band order alters owing to the symmetry breaking between the spinel $\gamma\text{-Al}_2\text{O}_3$ and perovskite SrTiO_3 . The band-order engineering exploiting the fundamental symmetry properties emerges as another route to boost the performance of oxide devices.

Keywords: transition-metal oxides, heterostructures, photoelectron spectroscopy, electronic band structure, electron-phonon interactions

The rich interplay of spin, orbital and lattice degrees of freedom in transition metal oxides (TMOs) results in a variety of unconventional phenomena, ranging from superconductivity to ferroelectricity, colossal magnetoresistance and ferromagnetism, which can be further enriched by interfacing these materials. A paradigm example is the two-dimensional electron system (2DES) that can spontaneously form at the interface between two perovskite band insulators LaAlO_3 (LAO) and SrTiO_3 (STO), for reviews see Refs. ^{1,2}. This interface combines many intriguing and even mutually exclusive properties such as superconductivity and ferromagnetism.³ Field-effect tunability of these properties^{2,4} allows realization of superconducting field-effect transistors and switchable magnetic states. Whereas the electron concentration (n_s) accumulated by the TMO interfaces is typically a couple of orders of magnitude larger compared to the semiconductor interfaces, the electron mobility (μ_e) still stays a few orders of magnitude less.⁵ In order to bring the functionality of the TMO interfaces to the level adequate for high-performance practical devices, this fundamental electron transport characteristic needs to be much improved. The limiting factors here include defect scattering, electron-correlation phenomena and, for the STO-based interfaces in particular, strong electron-phonon interaction (EPI) resulting in polaronic nature of the interfacial charge carriers.⁶

Different routes to increase μ_e of the TMO systems can be envisaged. The most common one is the so-called defect engineering, where the sample preparation procedure is tuned to reduce the concentration of defect scattering sites, including the oxygen vacancies (V_{O} s) or, in the spirit of the semiconductor high-electron-mobility transistors (HEMTs),^{7,8} shift their distribution away from the itinerant electrons. An example of such an approach is a modulation-doped heterostructure where a LaMnO_3 buffer layer is inserted between amorphous LAO and STO⁹ which not only reduces the concentration of V_{O} s on the STO side, but also serves as a spacer to increase the spatial separation between the electrons and the scattering sites.

Recently, the epitaxial heterostructure of spinel $\gamma\text{-Al}_2\text{O}_3$ (GAO) deposited on perovskite STO was found to exhibit extremely high μ_e values of up to 140,000 cm^2/Vs compared to around 1,000 cm^2/Vs in a typical LAO/STO heterostructure.¹⁰ This qualifies GAO/STO as the highest- μ_e TMO system after the ZnO-based ones.¹¹ Understanding the fundamental physics behind this μ_e -boost will be extremely important for further progress of the TMO-based devices. A recent photoemission study of GAO/STO supported by first-principles calculations¹² suggested an efficient diffusion of

V_O s from the STO bulk to the interface, reducing defect scattering of electrons deeper in STO. However, as the lowest-energy electron states in typical STO-based heterostructures are the d_{xy} ones located in the V_O -rich top TiO_2 layer,^{4,13} it remained unclear why the d_{xy} electrons did not spoil the overall μ_e . Intriguingly, later X-ray linear dichroism (XLD) experiments at the Ti 2*p* absorption edge^{14,15} have suggested a change in the band order in GAO/STO heterostructures, where the d_{xy} states shift above the $d_{xz/yz}$ ones, in contrast to the usual $d_{xz/yz} > d_{xy}$ band order at most STO-based interfaces. However, those experiments could not determine the \mathbf{k} -resolved bandstructure of the 2DES and, most importantly, they probed only the unoccupied states not directly involved in electron transport. Furthermore, the driving force of such band-order anomaly and its connection with the μ_e -boost stayed unclear.

Here, we explore the factors of the μ_e -boost in GAO/STO from direct measurements of the \mathbf{k} -resolved electronic structure of the buried 2DES, as schematized in Fig. 1, using resonant soft-X-ray angle-resolved photoelectron spectroscopy (ARPES) at the Ti 2*p* edge. The experiment reveals an anomalous band order, where the d_{xy} band shifts above the $d_{xz/yz}$ ones and depopulates. We reveal that this anomaly shifts the overall electron density away from the V_O -rich top STO layer, and the subsequent reduction of the effective defect concentration and the EPI strength, experienced by the mobile electrons, boosts μ_e . A crystal-field (CF) analysis for the interfacial Ti atoms shows that the band-order anomaly is caused by symmetry breaking at the non-isomorph spinel/perovskite interface of GAO/STO. Our analysis puts forward a yet unexplored avenue of the band-order engineering using symmetry breaking to tune properties of the TMO heterostructures towards particular device functionalities.

Results

The GAO/STO samples were grown by Pulsed Laser Deposition (PLD) under different oxygen pressure resulting in different n_s (see Methods).^{16,17} We have investigated a sample having low $n_s \sim 3 \times 10^{13} \text{ cm}^{-2}$ and $\mu_e \sim 12,000 \text{ cm}^2/\text{Vs}$ at 2 K, and another one having high $n_s \sim 6 \times 10^{14} \text{ cm}^{-2}$ and $\mu_e \sim 100,000 \text{ cm}^2/\text{Vs}$ at 2 K, with such dramatic variations of n_s and μ_e being typical of STO-based systems. The simultaneous increase of n_s and μ_e is a hallmark of GAO/STO. Our soft-X-ray ARPES experiments (see Methods) focused on the fundamental electronic structure characteristics – Fermi surface (FS), band dispersions and band order, spectral function – of the

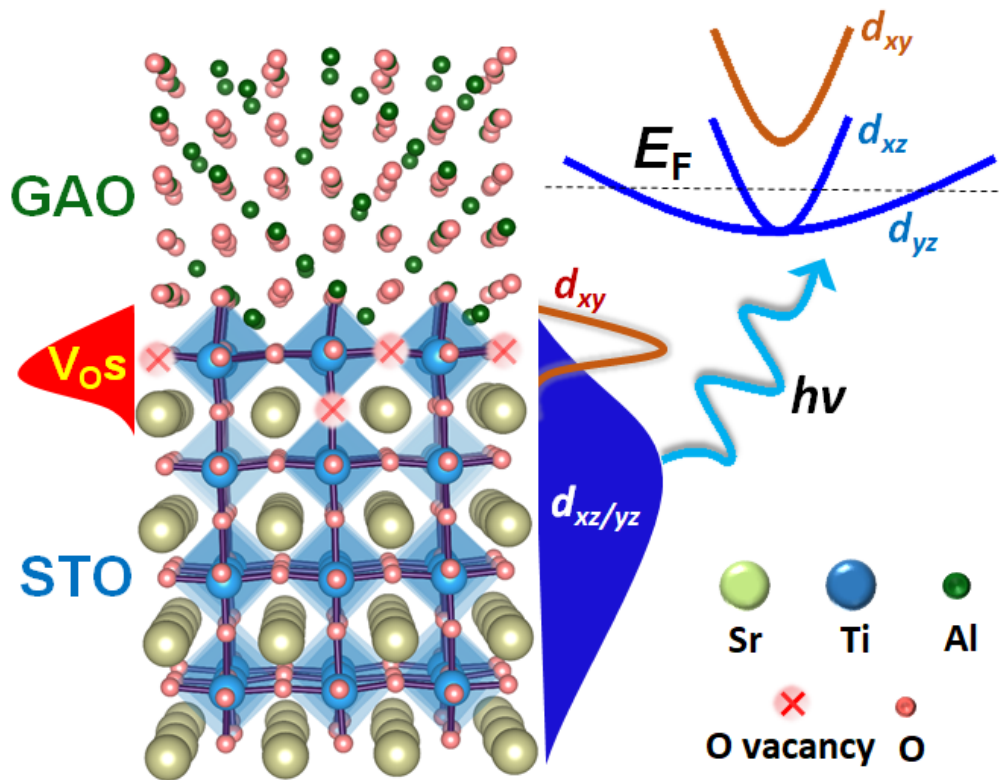


Fig. 1. Scheme of the GAO/STO interface probed with k -resolved photoemission to directly image electron dispersions. The ARPES experiment finds the band-order anomaly $d_{xy} > d_{xz/yz}$ which promotes spatial separation of the V_{O_s} from the 2DES to boost μ_e .

interfacial 2DES in these samples compared side-by-side with the paradigm LAO/STO interface irradiated by X-rays to create V_{O_s} . Both systems are oxygen-deficient with the V_{O_s} concentrated in the top STO layer^{18,19} (for more on electronic structure of the localized V_{O_s} -derived IG states in GAO/STO see the Supporting Information (SI) and the references therein). To access the buried Ti t_{2g} -derived 2DES in our samples, we used resonant photoexcitation at the Ti L_3 -edge at photon energy ($h\nu$) of 460.4 eV. First, we will analyze bandstructure of the 2DES states in terms of electron orbitals.

k-resolved electronic structure: Band-order anomaly

Fig. 2 (a) presents experimental ARPES image of the band dispersions along the ΓX direction of the Brillouin zone for our LAO/STO sample measured with s-polarized incident X-rays, selecting the antisymmetric d_{xy} and d_{yz} states. The out-of-plane d_{yz} states show their characteristic

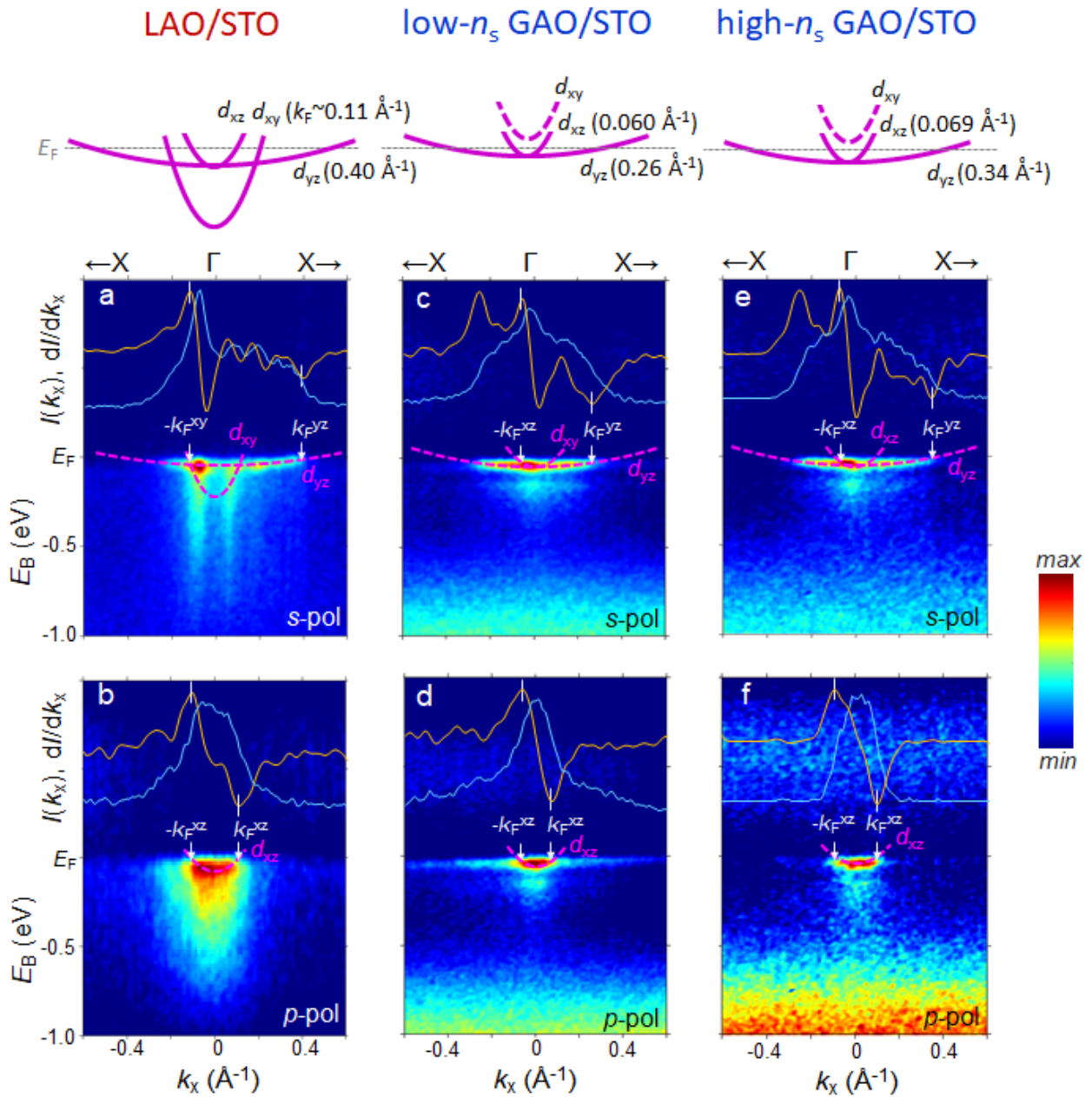


Fig. 2. Experimental $E(k)$ images along ΓX for the oxygen-deficient LAO/STO interface (a,b) and low- and high- n_s GAO/STO interfaces (c,d and e,f, respectively) measured at $h\nu = 460.4$ eV. For LAO/STO, s-polarized X-rays select the d_{xy} - and d_{yz} bands (top panels) and p-polarized X-rays the d_{xz} bands (bottom panels), and for GAO/STO these selection rules relax. The MDCs at E_F (cyan curves) and their gradients (yellow) are shown on top of each panel, with extremes of the latter (dashes) locating the k_F values (arrows). The sketches on top of the figure schematize the band order for the three samples, where GAO/STO shows the anomalous $d_{xy} > d_{xz/yz}$ band order with complete depopulation of the d_{xy} band.

flat dispersion, whereas the in-plane d_{xy} one have only a minute cross-section at high excitation energies²⁰ and is visible mostly in the points where it hybridizes with the d_{yz} states. Fig. 2 (b) represents the ARPES data measured with p -polarized X-rays, selecting the symmetric d_{xz} states.^{21,22} We note pronounced satellites below the band dispersions, identifying the polaronic nature of the interfacial charge carriers.^{6,22}

Importantly, the experimental bandstructure of LAO/STO follows the $d_{xy} < d_{xz/yz}$ band order, with the d_{xy} band minimum shifted by ~ 200 meV below that of $d_{xz/yz}$.¹⁹ Schematized on top of Fig. 2 (a), such pattern confirms the theoretical picture where the CF in bulk STO lowers the energy of Ti t_{2g} bands relative to the e_g ones, and interfacing STO with LAO further splits the former into the deeper d_{xy} -derived band and more shallow d_{xz}/d_{yz} ones.²¹⁻²³ The d_{xy} states are located close to the interface, while the d_{xz}/d_{yz} ones extend into the STO bulk over a region of up to a few tens nanometers, depending on the exact shape of the interfacial quantum well $V(\mathbf{r})$.^{4,6,13} The $d_{xy} < d_{xz/yz}$ band order observed in LAO/STO is actually universal across a wide range of systems based on TiO_2 -terminated STO almost independently of the growth conditions and oxygen deficiency. It starts from the paradigm LAO/STO interface²¹ and survives under amorphous overlayers of LAO,^{24,25} Si ²⁶ and a variety of metals²⁷⁻²⁹ on STO as well as for bare STO surfaces prepared under various conditions^{30,31} and even reconstructed by sputtering/annealing.³² This band order can though be tuned by applying pressure³³ or changing crystallographic orientations,³⁴ although the latter also changes the $d_{xy}/d_{xz}/d_{yz}$ orbital orientation relative to the surface or interface.

For GAO/STO, the experimental bandstructure of the d_{xy} - and d_{yz} states shown in Fig. 2 (c) and (e) for the low- and high- n_s samples, respectively, appears quite differently from LAO/STO. First of all, the proximity of GAO breaks the fourfold symmetry of STO due to the interfacial Ti cations which neighbor the tetrahedrally coordinated Al cations. Due to the concomitant relaxation of the above selection rules, at the s -polarization we observe certain weight of the d_{xz} band on top of the d_{yz} one (c,e), and at the p -polarization certain weight of the d_{yz} band on top of the d_{xz} one (d,f). Most importantly, the d_{xy} - d_{yz} hybridization points characteristic of LAO/STO disappear, indicating the absence of the d_{xy} band which has shifted above E_F and depopulated. This bandstructure pattern, schematized on top of the figure, identifies an anomalous $d_{xy} > d_{xz/yz}$ band order as opposed to the universal $d_{xy} < d_{xz/yz}$ one represented by the above LAO/STO. The intensity

enhancement at the bottom of the GAO/STO images is due to the V_O -derived IG states (see the SI). We note that the band-order is associated with a small change of the effective mass of the $d_{xz/yz}$ bands (see the SI) which, as we discuss later, can be related to the reduction of the EPI.

Therefore, our ARPES results reveal that electron transport in GAO/STO is exclusively due to the $d_{xz/yz}$ -electrons. We note that in many cases one can deduce the partial band occupancy from non-linearity of the Hall coefficient as a function of magnetic field. In the case of high-mobility GAO/STO samples, however, the Hall coefficient shows a very pronounced anomalous Hall effect stemming from the magnetism, and the concomitant non-linearity hides possible multiband effects. ARPES, in turn, clearly resolves the orbital character of the contributions to the total n_s .

We note that our ARPES findings of the anomalous band order in GAO/STO are consistent with the recent XLD experiments^{14,15} which are though relevant for the band order in the unoccupied states not directly related to the electron transport. Ionic liquid gating experiments¹⁷ suggested the persistence of the universal band order in GAO/STO, but these experiments probe the band structure only indirectly and may be affected by electrochemical reactions.

The Fermi momenta (k_F) of the experimental bands, reflecting their population, were determined from the momentum-distribution curves (MDCs) of the ARPES intensity $I(k_x)$ integrated over the whole occupied energy width (W) of the bands (cyan lines in the bandstructure panels of Fig. 2). The extremes of their gradient dI/dk_x (yellow lines) define the k_F values indicated at the band schemes on top of Fig. 2. We have utilized this gradient method originally proposed by Straub et al.³⁵ because in our case, where W is of the order of the experimental ΔE , the conventional determination of k_F from the maxima of the MDCs at E_F becomes obviously irrelevant. Assigning the dI/dk_x extremes to particular k_F , we should keep in mind that at the negative- k_x side of the d_{yz} bands and positive- k_x side of the d_{xy} ones the spectral intensity vanishes due to photoemission matrix elements. Inspecting the experimental k_F , we observe that not only does the d_{xy} band depopulate when going from LAO/STO to GAO/STO, but also the $d_{xz/yz}$ bands reduce their population; these bands increase their population between the low- to high- n_s GAO/STO samples. The relation of these observations with n_s and μ_e of the 2DES will be discussed later.

Symmetry-breaking origin of the band-order anomaly

In order to get more insight into the origin of the band-order anomaly at the spinel-perovskite GAO/STO interface, we have theoretically analyzed the CF splitting effects in the

ion-core regions of the interfacial Ti atoms. The CF potential was modeled for different atomic environments depicted in Fig. 3 (a,b). The point-charge approximation is used to calculate the spatial distribution of the electrostatic potential of N ions with nominal charges Q_i and coordinates r_i acting on electrons:

$$V_{CF}(\mathbf{r}) = - \frac{1}{4\pi\epsilon_0} \sum_{i=1}^N \frac{Q_i}{|\mathbf{r} - \mathbf{r}_i|}$$

The $3d$ states are approximated by the atomic orbitals with $n=3$ and $l=2$, which are used for evaluating the CF matrix:

$$H_{CF} = \langle nlm_1 | V_{CF}(r) - V_{CF}(0) | nlm_2 \rangle.$$

Here, $|nlm\rangle$ stands for spherical harmonics, the values of m_1 and m_2 are between -2 and $+2$ and correspond to d_{z^2} , $d_{x^2-y^2}$, d_{xy} , d_{xz} and d_{yz} orbitals. Diagonalization of the CF matrix H_{CF} gives information on the band ordering at the Γ -point for the selected atomic structure.

For the cubic STO atomic environment, Fig. 3 (a), the d_{xy} vs $d_{xz/yz}$ orbitals are degenerate. The degeneracy can be lifted, for example, by symmetry breaking when interfacing STO to other TMOs such as LAO, or by oxygen octahedra tilting. The latter, illustrated in Fig. 3 (c) where the tilting around the x - or y -axes pushes the d_{yz} or d_{xz} states above the d_{xy} one, is typical of TMOs and constitutes one of the contributions to the interfacial potential in oxide heterostructures. The symmetry breaking and oxygen-octahedra tilting, both lead to a shift of the $d_{xz/yz}$ orbitals above the d_{xy} one, Fig. 3 (c), which was, indeed commonly observed as the universal band order in numerous experimental and theoretical studies of STO-based interfaces.^{19,21,36,37}

For the spinel-perovskite environment, Fig. 3(b), we find that the CF energy levels are dramatically rearranged due to the proximity of positively charged Al cations, which can be either octahedrally or tetrahedrally coordinated by oxygen. The particular coordination is crucial for the energy position of the IG states in GAO/STO formed by the V_{O_s} s, but does not qualitatively change the anomalous band order of the metallic states which stays inverse compared to LAO/STO. Our CF calculations suggest that the lowest energy level becomes dominated by the d_{xz}/d_{yz} states that are mixed in 1:1 ratio while the next higher energy levels are mostly of the $+d_{xy}$ character, Fig. 3 (d). We emphasize that this feature is robust with respect to whether the Al vacancies, intrinsically present in GAO, are located in the Al-layer close to STO or elsewhere in GAO. In the studied example, the V_{O_s} increase the energy separation between the d_{xy} and $d_{xz/dyz}$ orbitals slightly but do not

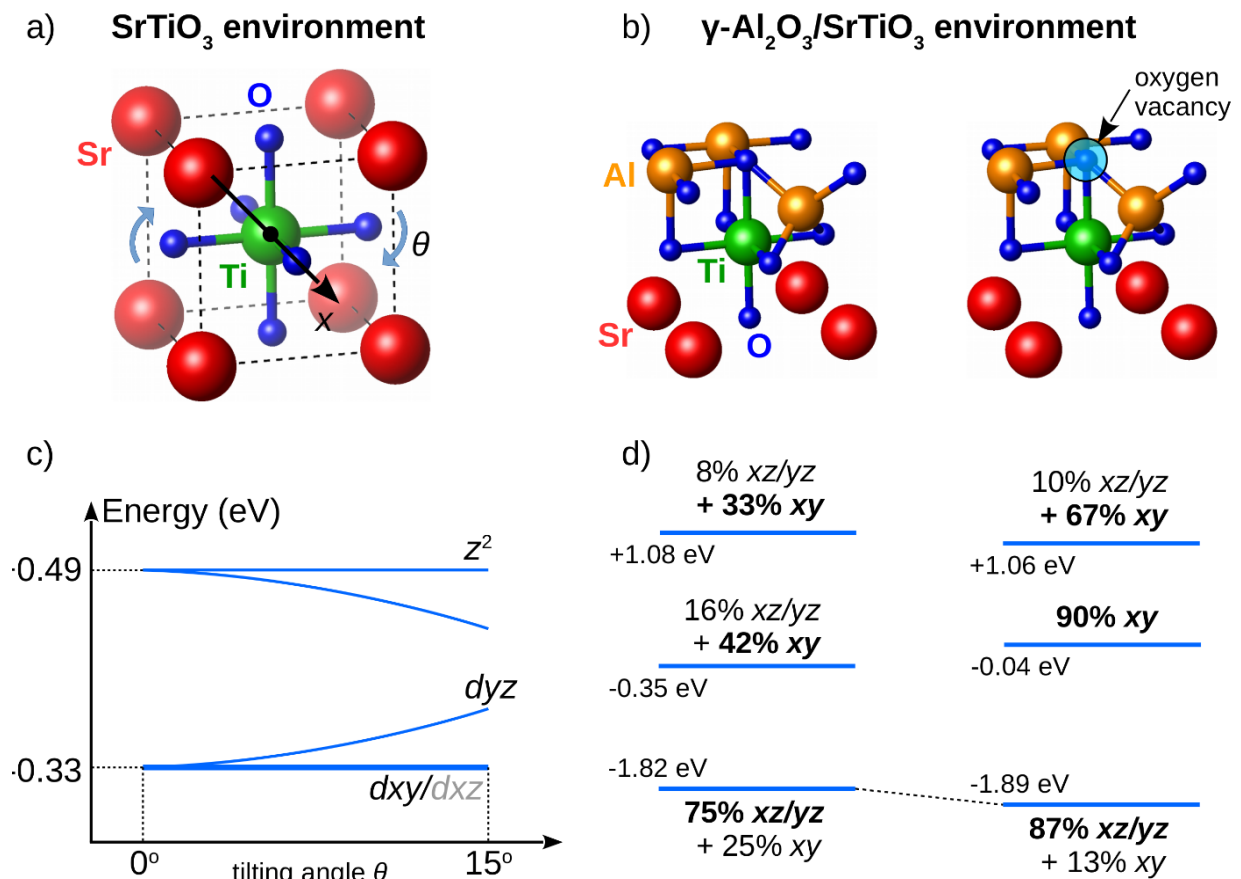


Fig. 3. CF analysis for different atomic environments. a) Structural sketch of bulk perovskite STO. b) Structural sketch of one possible termination of the spinel-perovskite GAO/STO interface. c) CF energy levels for bulk STO as a function of the oxygen octahedra tilting angle. d) Lowest CF energy levels for defect-free and oxygen-deficient GAO/STO environments, with the orbital character and weights indicated (the dominant weight in bold).

change this picture qualitatively, simply providing electrons filling energy levels. Therefore, our analysis suggests that the band-order anomaly in GAO/STO originates from the different nature of the CF in the ion-core regions of the interfacial Ti atoms at this spinel-perovskite interface compared to the perovskite-perovskite LAO/STO one.

Spectral function: Electron-phonon interactions and disorder

We will now analyze another important ingredient of the electronic properties, the EPI, which is embedded in the spectral function $A(\omega, \mathbf{k})$ represented by the energy-distribution curves

(EDCs) of the ARPES intensity in Fig. 2. Similarly to the previous analysis for the stoichiometric LAO/STO,^{6,22} we will use $A(\omega)$ obtained by integration of $A(\omega, \mathbf{k})$ over the whole $\pm k_F$ interval of the d_{yz} bands. This approach allows full inclusion of the bosonic spectral satellites whose extension in \mathbf{k} -space may be narrower than the quasiparticle (QP) bands.³⁸ The experimental $A(\omega)$ for our oxygen-deficient LAO/STO and both GAO/STO samples (where we subtracted the IG state weight protruding into the 2DES energy region) are presented in Fig. 4 (a). Their pronounced peak-dip-hump lineshape is a hallmark of the strong EPI in STO-based systems, fundamentally reducing μ_e .^{6,22} We recall that whereas for LAO/STO the $A(\omega, \mathbf{k})$ reflects both d_{xy} and $d_{xz/yz}$ states, for GAO/STO it reflects only the latter.

For LAO/STO the hump is structureless and extends over a wide energy range, suggesting a continuum of phonon modes involved in the EPI. For GAO/STO, in contrast, the hump is a narrow peak separated from the QP one by ~ 100 meV which corresponds to the LO3-phonon energy in STO.³² The increase of the QP residual weight Z_0 from $\sim 31\%$ in LAO/STO to $\sim 45\%$ in GAO/STO signals a decrease of the EPI strength in the latter. Expectedly, this increase is associated with a notable reduction of the effective mass of the $d_{xz/yz}$ bands (see the SI) although a limited accuracy of its experimental values impedes a quantitative analysis on this point.

Finally, we will analyze the disorder experienced by the charge carriers. Fig. 4 (b) presents the QP peak in vicinity of E_F whose $A(\omega, \mathbf{k}=\mathbf{k}_F)$ was obtained as EDCs integrated within $\pm 0.1 \text{ \AA}^{-1}$ around k_F of the d_{yz} bands. In this case the band-dispersion effects are minimized and, within the Fermi-liquid paradigm, the spectral broadening due to electron-electron interaction vanishes at E_F . Therefore, the QP-peak broadening (ΔE) which, neglecting the experimental energy resolution, is inversely proportional to the coherence length of the charge carriers, reflects the effective disorder they experience. In comparison with the LAO/STO's value $\Delta E \sim 62$ meV, for the GAO/STO samples we observe $\Delta E \sim 50$ meV, which is close to the resolution limit ~ 40 meV of our experiment. The reduced ΔE expresses the smaller effective disorder experienced by the d_{yz} -derived charge.

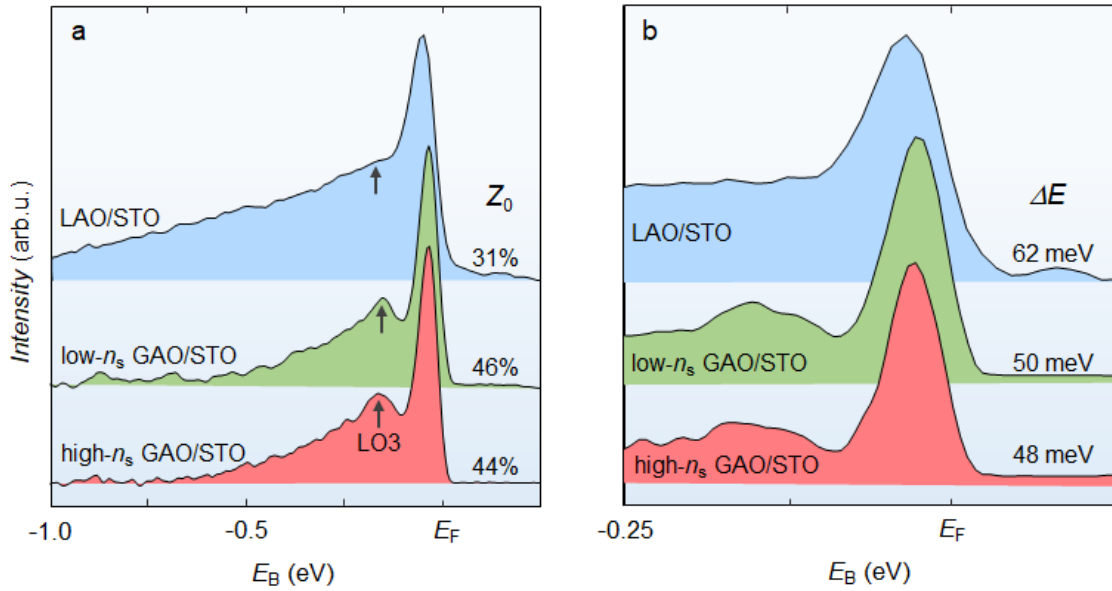


Fig. 4. Experimental $A(\omega, \mathbf{k})$ for oxygen-deficient LAO/STO and two GAO/STO samples represented by EDCs of the ARPES intensity from Fig. 2 integrated over the (a) whole $\pm k_F$ interval and (b) $k_F \pm 0.1 \text{ \AA}^{-1}$ interval. Compared to LAO/STO, in both GAO/STO samples the QP peak shows larger spectral weight Z_0 and smaller energy broadening ΔE (values on the plots) which identify weaker EPI and smaller effective disorder, respectively.

Discussion

Effect of the band order on μ_e

The central question is now how does the observed band-order anomaly affect μ_e ? Fig. 1 sketches the distribution of the V_{O} s relative to the depopulated d_{xy} and populated $d_{xz/yz}$ electron density in GAO/STO. The V_{O} s effectively diffuse to the top STO layer, reducing their concentration and thereby the associated defect scattering in the deeper STO region.¹² This reduction is confirmed by our analysis of the QP peak width from the $d_{xz/yz}$ -electrons extending into this region, which has evidenced a small effective disorder experienced by these electrons compared to LAO/STO. Located in the defect-free region, the $d_{xz/yz}$ -electrons deliver high $\mu_e^{xz/yz}$, whereas the d_{xy} -states, located in the defect-rich top layer,^{4,13,21} are depopulated and thus do not poison the overall μ_e . This interplay between the spatial distribution and population of the electron states is the main driving force behind the boost of μ_e in GAO/STO. Obviously, the boost critically depends on

the spatial distribution of the V_{O} s and other defect sites, highly sensitive to the sample growth and annealing protocol.¹²

The $d_{xy} > d_{xz/yz}$ band order will affect virtually all the properties of the GAO/STO besides μ_e . For example, it should reverse the sign of the gating voltage corresponding to the Lifshitz transition, where the crossover from the one-band to multiband regime causes dramatic changes in physical properties of the STO-based heterostructures including the superconducting transition temperature, electron pairing strength, and spin-orbit coupling.³⁹ Moreover, our ARPES findings may also have implications for the mechanism of superconductivity in GAO/STO, as this phenomenon in the STO-based systems is usually observed in the multiband conduction regime.⁴⁰ Both points still await experimental verification though.

Depth extension of the 2DES

The connection of the ARPES data to the carrier density is established by the Luttinger theorem.⁴¹ For the 2D systems, it states that n_s is equal to the sum of the partial Luttinger counts

$$2 \int_{FS} \frac{d^2k}{(2\pi)^2}$$

over all sheets constituting the FS. However, the application of this theorem to our case is not straightforward even knowing the experimental FS of GAO/STO (see the SI). Firstly, a typical feature of the STO-based systems is the electronic phase separation where conducting regions co-exist with insulating ones.^{18,42,43} While experimental FS reflects the local electron density in the conducting areas, the integral n_s can be smaller. Secondly, if the interfacial $V(\mathbf{r})$ is sufficiently long-range, it hosts a ladder of quantum-well (QW) states,⁴⁴ and the Luttinger count should include the FS sheets through all of them. However, whereas the first QW state is located close to the interface, the higher-order ones are shifted deeper into the STO bulk⁴⁵ where they can escape detection within the probing depth of the ARPES experiment while contributing to the total n_s . Because of the missing higher-order FS sheets, the Luttinger count of the FS apparent in ARPES may underestimate the n_s measured in transport.

Intriguingly, the experimental \mathbf{k}_F values found by ARPES for GAO/STO show an increase of the corresponding Luttinger counts by only $\sim 15\%$ between the low- and high- n_s samples, which is much less compared to the increase of transport n_s by a factor of ~ 20 . This discrepancy may manifest the two effects discussed above. First, the lateral increase of the conducting phase

between the low- and high- n_s samples, estimated from intensity of the 2DES signal as described in Ref. ¹⁸, measures ~70%. The remaining contribution to the n_s increase of more than an order of magnitude should then manifest a long-range $V(\mathbf{r})$ in the high- n_s sample, which supports an electron-density accumulation in higher-order $d_{xz/yz}$ derived QW states located in STO beyond the top 2-3 u.c. reached by ARPES. This situation can be viewed as a transformation of the 2DES into a quasi-three-dimensional system expanding deep into V_O -free STO. In this case the increase of n_s should be associated with an increase of μ_e , and it indeed increases by a factor of ~8 between our samples. This physical picture resolves the long-standing puzzle why GAO/STO denies the 'small n_s - large μ_e ' paradigm often advocated for oxide interfaces, although other cases have been reported where this paradigm was violated by similar dimensionality transformations.⁴⁶

Effects of the EPI

The weakening of the EPI, expressed by the Z_0 values in Fig. 4 (a), is another aspect of GAO/STO contributing to the μ_e -boost. For many systems such weakening is caused by screening of the EPI by mobile electrons. In our case, however, ARPES shows that at least near the interface the $d_{xz/yz}$ derived electron density in GAO/STO is smaller than the $d_{xz/yz}$ (and all the more $d_{xy}+d_{xz/yz}$) density in our LAO/STO. In fact, the EPI may be amplified by trapping (localization) of charge carriers on defects⁴⁷ or *via* more exotic Anderson localization.⁴⁸ This lowers the crystal symmetry, allowing otherwise prohibited phonon modes and thus additional EPI channels. The involvement of such localization-enhanced EPI in our case is evident from the phonon-mode continuum displayed by LAO/STO's $A(\omega)$ as opposed to the single mode in GAO/STO. Then the reduction of the effective defect concentration in GAO/STO, expressed by the smaller disorder seen in the QP-peak width, Fig. 4 (b), explains the reduction of the EPI. This effect traces back, again, to the band-order anomaly that shifts the total 2DES into the V_O -free bulk of STO. The small but significant decrease of EPI in the high- n_s GAO/STO sample compared to the low- n_s one should be a combined effect of smaller effective disorder due to the deeper expansion of the 2DES into STO, and of larger n_s screening the EPI.

The observed weakening of EPI in GAO/STO propagates into μ_e not only by polaronic renormalization of the electron effective mass, but also by mediating electron scattering on defects, which can somehow be viewed as frozen phonons. Therefore, the defects affect μ_e not only through their concentration but also through the EPI-mediated electron-defect scattering strength

which, in turn, increases with the defect concentration. This cumulative effect results in a steep non-linear change of μ_e as a function of the latter, predicted within the mean-field approximation already four decades ago⁴⁹ and later reproduced by approximation-free Diagrammatic Monte Carlo calculations.^{50–52} This effect is likely to be at play to boost μ_e with decrease of the effective V_O concentration experienced by the $d_{xz/yz}$ electrons in GAO/STO thanks to the band-order anomaly. Indeed, this decrease is evident from our analysis of the QP peak width in Fig. 4 (b). The tendency of V_O s to cluster¹⁸ can also affect μ_e .

Conclusions and outlook

To summarize our results, we have found that the \mathbf{k} -resolved electronic structure of the 2DES at the GAO/STO interface stands out of all other known STO-based interfaces in terms of the band order. The upward shift of the d_{xy} -states with respect to the d_{xz}/d_{yz} ones, forming the anomalous $d_{xy} > d_{xz/yz}$ band order and depopulating the d_{xy} band, is attributed to a change in the CF configuration around the Ti ions as the spinel/perovskite GAO/STO interface breaks the perovskite-lattice symmetry. The band-order affects virtually all physical properties of GAO/STO, and in the first place boosts μ_e of the interfacial 2DES which shifts away from the defect-rich interface towards the STO bulk.

The μ_e -boost at the GAO/STO interface appears as a multifaceted phenomenon, identifying three routes to design high-mobility oxide devices in general: (1) The static defects, in particular the V_O s, affect μ_e through low-temperature electron scattering. With inspiration from the semiconductor HEMTs, this scattering can be reduced by shifting the depth profile of V_O s away from that of the 2DES to minimize their overlap. In GAO/STO this is achieved by the accumulation of the V_O s at the top TiO_2 layer of STO away from the 2DES located deeper in STO¹². The crucial role of this *defect-engineering* route for GAO/STO can be assessed by varying the growth protocol and thus distribution of V_O s;⁵³ (2) This work suggests the second route, *band-order engineering*. Complementary to the defect engineering, this route allows control over the 2DES depth profile in order to shift it away from the V_O s. In GAO/STO this is achieved with the $d_{xy} > d_{xz/yz}$ band order, which depopulates the d_{xy} states and leaves only the $d_{xz/yz}$ -electrons, located deeper in the STO bulk compared to the d_{xy} ones in the defect-rich top layer. Moreover, the increase of n_s in GAO/STO expands the 2DES into the STO bulk and thus further increases μ_e . The band order can be

manipulated through the CF driven by the interface-symmetry breaking and, in addition, tuned by doping such as substituting Al^{3+} ions in GAO with those of a dissimilar valence state; (3) The third route to boost μ_e is the *EPI-engineering* route that invokes the EPI-mediated electron interaction with the defects. As the EPI itself is enhanced by electron trapping on the defects, the resulting μ_e shows a steep non-linear dependence of their effective concentration, in our case that of the V_{O} s over the 2DES spatial extension. In this context the EPI-engineering is intimately connected with the defect and band-order engineering. The EPI can also be tuned through n_s varied, for example, by electrostatic gating.⁵⁴ Thereby, the GAO/STO interface teaches us a triad of interconnected routes – defect-, band-order and EPI-engineering – towards realization of a high-mobility 'oxide HEMT'. None of them alone but only the whole triad, and perhaps assisted by other yet unknown mechanisms, can exhaust the entire μ_e -boost in GAO/STO of more than two orders compared to the paradigm LAO/STO heterostructures.

In a broader perspective, the crucial role of the band-order engineering extends from merely electron transport towards the whole world of other exotic properties of the oxide systems including gate-tunable superconductivity, Lifshitz transition, electron pairing without superconductivity, spin-orbit coupling, magnetic ordering, *etc.* For example, the $d_{xy} > d_{xz/yz}$ band order observed in GAO/STO should revert the gate-voltage sign of the Lifshitz transition as well as switch the superconductivity from the multiband to one-band regime. Our work puts forward a prospect to change the band order through an appropriate lattice-symmetry breaking, and tuning the CF splitting by dopants of a dissimilar valence state or by (pseudo) epitaxial growth of other members of the large spinel crystal family. Our findings motivate searching of other oxide interfacial pairs, where the d_{xy} bands totally depopulate to maximize μ_e , using modern big-data computational methods.

Methods

Sample fabrication and characterization

The samples were manufactured by pulsed laser deposition (PLD) on STO substrates. The reference LAO/STO samples were grown in slightly oxygen-deficient conditions and annealed in oxygen *ex-situ*, following the protocol described in Refs. ^{18,19}. The GAO/STO samples were manufactured using the protocol described elsewhere¹⁶ under the oxygen partial pressure varied from 4 to 8×10^{-6} mbar in order to change the transport properties through the V_{O} concentration. The

two investigated GAO/STO samples were metallic with low $n_s \sim 3 \times 10^{13} \text{ cm}^{-2}$ and high $n_s \sim 6 \times 10^{14} \text{ cm}^{-2}$ at room temperature with the residual resistance ratio $R_s(300\text{K})/R_s(2\text{K})$ of ~ 1100 and 9300 , respectively. The high residual resistance ratios are the hallmarks of samples with high low-temperature μ_e ,¹⁶ which was $\sim 12,000 \text{ cm}^2/\text{Vs}$ and $100,000 \text{ cm}^2/\text{Vs}$ at 2 K for the two samples.

ARPES experiment

The experiments were performed at the soft-X-ray ARPES facility⁵⁵ installed at the ADRESS beamline⁵⁶ of the Swiss Light Source, Paul Scherrer Institute, Switzerland. Variable X-ray polarization delivered by this beamline allowed symmetry analysis of the electron states. The FS maps were recorded at a combined (beamline plus analyzer PHOIBOS-150) energy resolution of $\sim 60 \text{ meV}$, and $E(\mathbf{k})$ maps at $\sim 40 \text{ meV}$. Angular resolution of the analyzer was $\sim 0.1^\circ$. The sample was cooled down to $\sim 12\text{K}$ in order to quench relaxation of \mathbf{k} -conservation due to thermal motion of the atoms. The photon flux was $\sim 10^{13} \text{ photons/s}$ and focused into a spot of $30 \times 75 \mu\text{m}^2$ on the sample surface. Other relevant experimental details are reported elsewhere.^{6,19}

During the ARPES data acquisition, the strength of the 2DES signal from our LAO/STO and GAO/STO samples gradually increased because the V_{O} s generated under X-ray irradiation injected mobile electrons into the 2DES.^{18,19} However, the observed band dispersions and population stayed constant, following the electronic phase separation scenario typical of the STO-based systems.^{18,20,42,43} The irradiation-induced increase of the 2DES signal from the high- n_s GAO/STO sample was smaller compared to the low- n_s one. All reported ARPES data were acquired after an irradiation time of more than 1 hour to insure saturation. The experimental resonant-photoemission intensity maps as a function of $h\nu$ through the Ti L -edge for our LAO/STO and low- n_s GAO/STO samples are presented in the SI. Intensity of the V_{O} -derived IG states at a binding energy around -1.2 eV and of the 2DES states near E_{F} sharply varied with $h\nu$. The data in the main text have been acquired at the L_3 -resonance at $h\nu = 460.4 \text{ eV}$, where the d_{xy} -to- $d_{xz/yz}$ intensity ratio enhances compared to the L_2 -resonance.^{6,19} The corresponding FS maps of GAO/STO measured at different X-ray polarizations are presented in the SI. Besides the reduced FS area, their notable difference to the FS maps of LAO/STO is notable streaks of intensity stretching between the Γ points. This peculiarity might be related to linear clusters of the interfacial V_{O} s or, although scanning-SQUID measurements on similarly prepared samples have found micron-size domains, the existence of

domains whose size would be below the coherence length of the ARPES experiment (for details see the SI).

Associated Content

The SI includes (1) Ti *L*-edge resonant photoemission data, (2) effective-mass analysis, (3) DFT calculations, and (4) experimental Fermi surface. The SI is available online.

Author information

Corresponding authors

Vladimir N. Strocov – *Swiss Light Source, Paul Scherrer Institute, 5232 Villigen-PSI, Switzerland*;
Phone: +41-56-310-5311; orcid.org/0000-0002-1147-8486; Email: vladimir.strocov@psi.ch

Nini Pryds – *Department of Energy Conversion and Storage, Technical University of Denmark, 2800 Kgs. Lyngby, Denmark*; orcid.org/0000-0002-5718-7924; Phone: +45-46-77-5752; Email: nipr@dtu.dk

Author contributions

A.C., D.C., Y.C., M.A.H., M.R., N.P. and V.N.S. performed the ARPES experiment assisted by X. W. and T.S. V.N.S, A.C., and M.A.H. processed the ARPES data. D.C. and Y.Z.C. supported by N.P. fabricated the samples and performed their transport characterization. V.N.S. and N.P. conceived the idea of the band-order effect on electron mobility, and A.S.M. supported by N.N. elaborated the physics of EPI. V.B. supported by R.V. performed the CF calculations. V.N.S. wrote the manuscript with contributions from A.C., D.C., V.B. and A.M. All authors discussed the results, interpretations, and scientific concepts.

Notes

The authors declare no competing financial or non-financial interests.

Acknowledgements

We thank L. Nue for skillful technical support of the SX-ARPES experiments. A.C. acknowledges funding from the Swiss National Science Foundation under Grant no. 200021-165529. M.-A.H. was supported by the Swiss Excellence Scholarship grant ESKAS-no. 2015.0257 and the Romanian UEFISCDI Agency under Contracts No. 475 PN-III-P4-ID-PCCF2016-0047. A.S.M. and N.N. acknowledge support of JST CREST Grant Number JPMJCR1874, Japan. V.B. and R.V. were supported by DFG Sonderforschungsbereich TRR 49 and by the computer center of Goethe University Frankfurt.

References

- (1) Hwang, H. Y.; Iwasa, Y.; Kawasaki, M.; Keimer, B.; Nagaosa, N.; Tokura, Y. Emergent Phenomena at Oxide Interfaces. *Nature Materials*. **2012**, *11*, 103–113.
- (2) Mannhart, J.; Schlom, D. G. Oxide Interfaces – An Opportunity for Electronics. *Science* **2010**, *327* (5973), 1607–1611.
- (3) Bert, J. A.; Kalisky, B.; Bell, C.; Kim, M.; Hikita, Y.; Hwang, H. Y.; Moler, K. A. Direct Imaging of the Coexistence of Ferromagnetism and Superconductivity at the LaAlO₃/SrTiO₃ Interface. *Nat. Phys.* **2011**, *7*, 767–771.
- (4) Gariglio, S.; Reyren, N.; Caviglia, A. D.; Triscone, J.-M. Superconductivity at the LaAlO₃/SrTiO₃ Interface. *J. Phys. Condens. Matter* **2009**, *21*, 164213.
- (5) Sulpizio, J. A.; Ilani, S.; Irvin, P.; Levy, J. Nanoscale Phenomena in Oxide Heterostructures. *Annual Review of Materials Research*. **2014**, *44*, 117–149.
- (6) Cancellieri, C.; Mishchenko, A. S.; Aschauer, U.; Filippetti, A.; Faber, C.; Barišić, O. S.; Rogalev, V. A.; Schmitt, T.; Nagaosa, N.; Strocov, V. N. Polaronic Metal State at the LaAlO₃/SrTiO₃ Interface. *Nat. Commun.* **2016**, *7*, 10386.
- (7) Mimura, T. The Early History of the High Electron Mobility Transistor (HEMT). *IEEE Transactions on Microwave Theory and Techniques*. **2002**, *50*, 780–782.
- (8) Lev, L. L.; Maiboroda, I. O.; Husanu, M.; Grichuk, E. S.; Chumakov, N. K.; Ezubchenko, I. S.; Chernykh, I. A.; Wang, X.; Tobler, B.; Schmitt, T.; Zhanavskina, M. L.; Valeev, V. G.; Strocov, V. N. **k**-Space Imaging of Anisotropic 2D Electron Gas in GaN/GaN High-Electron-Mobility Transistor Heterostructures. *Nature Communications*. **2018**, *9*, 2653
- (9) Chen, Y. Z.; Trier, F.; Wijnands, T.; Green, R. J.; Gauquelin, N.; Egoavil, R.; Christensen, D. V.; Koster, G.; Huijben, M.; Bovet, N.; Macke, S.; He, F.; Sutarto, R.; Andersen, N. H.; Sulpizio, J. A.; Honig, M.; Prawiroatmodjo, G. E. D. K.; Jespersen, T. S.; Linderoth, S.; Ilani, S. *et al.* Extreme Mobility Enhancement of Two-Dimensional Electron Gases at Oxide Interfaces by Charge-Transfer-Induced Modulation Doping. *Nat. Mater.* **2015**, *14*, 801–806.
- (10) Chen, Y. Z.; Bovet, N.; Trier, F.; Christensen, D. V.; Qu, F. M.; Andersen, N. H.; Kasama, T.; Zhang, W.; Giraud, R.; Dufouleur, J.; Jespersen, T. S.; Sun, J. R.; Smith, A.; Nygård, J.; Lu, L.; Büchner, B.; Shen, B. G.; Linderoth, S.; Pryds, N. A. High-Mobility Two-Dimensional Electron

Gas at the Spinel/Perovskite Interface of γ -Al₂O₃/SrTiO₃. *Nat. Commun.* **2013**, *4*, 1371.

- (11) Falson, J.; Kozuka, Y.; Uchida, M.; Smet, J. H.; Arima, T.-H.; Tsukazaki, A.; Kawasaki, M. MgZnO/ZnO Heterostructures with Electron Mobility Exceeding 1×10^6 cm²/Vs. *Scientific Reports.* **2016**, *6*, 26598.
- (12) Schütz, P.; Christensen, D. V.; Borisov, V.; Pfaff, F.; Scheiderer, P.; Dudy, L.; Zapf, M.; Gabel, J.; Chen, Y. Z.; Pryds, N.; Rogalev, V. A.; Strocov, V. N.; Schlueter, C.; -L. Lee, T.; Jeschke, H. O.; Valentí, R.; Sing, M.; Claessen, R. Microscopic Origin of the Mobility Enhancement at a Spinel/Perovskite Oxide Heterointerface Revealed by Photoemission Spectroscopy. *Physical Review B.* **2017**, *96*, 161409(R)
- (13) Delugas, P.; Filippetti, A.; Fiorentini, V.; Bilc, D. I.; Fontaine, D.; Ghosez, P. Spontaneous 2-Dimensional Carrier Confinement at the *N*-Type SrTiO₃/LaAlO₃ Interface. *Phys. Rev. Lett.* **2011**, *106*, 166807.
- (14) Cao, Y.; Liu, X.; Shafer, P.; Middey, S.; Meyers, D.; Kareev, M.; Zhong, Z.; Kim, J.-W.; Ryan, P. J.; Arenholz, E.; Chakhalian, J. Anomalous Orbital Structure in a Spinel–Perovskite Interface. *npj Quantum Materials.* **2016**, *106*, 166807.
- (15) Mardegan, J. R. L.; Christensen, D. V.; Chen, Y. Z.; Parchenko, S.; Avula, S. R. V.; Ortiz-Hernandez, N.; Decker, M.; Piamonteze, C.; Pryds, N.; Staub, U. Magnetic and Electronic Properties at the γ -Al₂O₃/SrTiO₃ Interface. *Physical Review B.* **2019**, *99*, 134423.
- (16) Christensen, D. V.; Frenkel, Y.; Schütz, P.; Trier, F.; Wissberg, S.; Claessen, R.; Kalisky, B.; Smith, A.; Chen, Y. Z.; Pryds, N. Electron Mobility in γ -Al₂O₃/SrTiO₃. *Physical Review Applied.* **2018**, *12*, 7927.
- (17) Niu, W.; Zhang, Y.; Gan, Y.; Christensen, D. V.; Soosten, M. V.; Garcia-Suarez, E. J.; Riisager, A.; Wang, X.; Xu, Y.; Zhang, R.; Pryds, N.; Chen, Y. Giant Tunability of the Two-Dimensional Electron Gas at the Interface of γ -Al₂O₃/SrTiO₃. *Nano Letters.* **2017**, *12*, 6878–6885.
- (18) Strocov, V. N.; Chikina, A.; Caputo, M.; -A. Husanu, M.; Bisti, F.; Bracher, D.; Schmitt, T.; Miletto Granozio, F.; Vaz, C. A. F.; Lechermann, F. Electronic Phase Separation at LaAlO₃/SrTiO₃ Interfaces Tunable by Oxygen Deficiency. *Physical Review Materials.* **2019**, *3*, 106001.
- (19) Chikina, A.; Lechermann, F.; Husanu, M.-A.; Caputo, M.; Cancellieri, C.; Wang, X.; Schmitt, T.; Radovic, M.; Strocov, V. N. Orbital Ordering of the Mobile and Localized Electrons at Oxygen-Deficient LaAlO₃/SrTiO₃ Interfaces. *ACS Nano.* **2018**, *12*, 7927–7935.

- (20) Strocov, V. N. Photoemission Response of 2D Electron States. *Journal of Electron Spectroscopy and Related Phenomena*. **2018**, 229, 100–107.
- (21) Cancellieri, C.; Reinle-Schmitt, M. L.; Kobayashi, M.; Strocov, V. N.; Willmott, P. R.; Fontaine, D.; Ghosez, P.; Filippetti, A.; Delugas, P.; Fiorentini, V. Doping-Dependent Band Structure of LaAlO₃/SrTiO₃ Interfaces by Soft X-Ray Polarization-Controlled Resonant Angle-Resolved Photoemission. *Physical Review B*. **2014**, 89, 121412(R).
- (22) Strocov, V. N.; Cancellieri, C.; Mishchenko, A. S. Electrons and Polarons at Oxide Interfaces Explored by Soft-X-Ray ARPES. *Spectroscopy of Complex Oxide Interfaces: Photoemission and Related Spectroscopies*; Springer Series in Materials Science 266; Springer: Cham, **2018**, 107–151.
- (23) Cancellieri, C.; Strocov, V. N. (Eds.) *Spectroscopy of Complex Oxide Interfaces: Photoemission and Related Spectroscopies*; Springer Series in Materials Science 266; Springer: Cham, **2018**.
- (24) Trier, F.; Amoruso, S.; Christensen, D. V.; Sambri, A.; Chen, Y. Z.; Wang, X.; Stamate, E.; Bruzzese, R.; Pryds, N. Controlling the Conductivity of Amorphous LaAlO₃/SrTiO₃ Interfaces by *in Situ* Application of an Electric Field during Fabrication. *Applied Physics Letters*. **2013**, 103, 031607.
- (25) Li, C.; Hong, Y.; Xue, H.; Wang, X.; Li, Y.; Liu, K.; Jiang, W.; Liu, M.; He, L.; Dou, R.; Xiong, C.; Nie, J. Formation of Two-Dimensional Electron Gas at Amorphous/Crystalline Oxide Interfaces. *Sci. Rep.* **2018**, 8, 404.
- (26) Chikina, A.; Caputo, M.; Naamneh, M.; Christensen, D. V.; Schmitt, T.; Radovic, M.; Strocov, V. N. Semiconductors: X-Ray Writing of Metallic Conductivity and Oxygen Vacancies at Silicon/SrTiO₃ Interfaces. *Advanced Functional Materials*. **2019**, 29, 1970172.
- (27) Rödel, T. C.; Fortuna, F.; Sengupta, S.; Frantzeskakis, E.; Le Fèvre, P.; Bertran, F.; Mercey, B.; Matzen, S.; Agnus, G.; Maroutian, T.; Lecoeur, P.; Santander-Syro, A. F. Universal Fabrication of 2D Electron Systems in Functional Oxides. *Adv. Mater.* **2016**, 28, 1976–1980.
- (28) Kormondy, K. J.; Gao, L.; Li, X.; Lu, S.; Posadas, A. B.; Shen, S.; Tsoi, M.; McCartney, M. R.; Smith, D. J.; Zhou, J.; Lev, L. L.; Husanu, M.-A.; Strocov, V. N.; Demkov, A. A. Large Positive Linear Magnetoresistance in the Two-Dimensional t_{2g} Electron Gas at the EuO/SrTiO₃ Interface. *Scientific Reports*. **2018**, 8, 7721.
- (29) Posadas, A. B.; Kormondy, K. J.; Guo, W.; Ponath, P.; Geler-Kremer, J.; Hadamek, T.;

- Demkov, A. A. Scavenging of Oxygen from SrTiO₃ during Oxide Thin Film Deposition and the Formation of Interfacial 2DEGs. *Journal of Applied Physics*. **2017**, *121*, 105302.
- (30) Sing, M.; Jeschke, H. O.; Lechermann, F.; Valentí, R.; Claessen, R. Influence of Oxygen Vacancies on Two-Dimensional Electron Systems at SrTiO₃-Based Interfaces and Surfaces. *The European Physical Journal Special Topics*. **2017**, *226*, 2457–2475.
- (31) Plumb, N. C.; Salluzzo, M.; Razzoli, E.; Månsson, M.; Falub, M.; Krempasky, J.; Matt, C. E.; Chang, J.; Schulte, M.; Braun, J.; Ebert, H.; Minár, J.; Delley, B.; -J. Zhou, K.; Schmitt, T.; Shi, M.; Mesot, J.; Patthey, L.; Radović, M. Mixed Dimensionality of Confined Conducting Electrons in the Surface Region of SrTiO₃. *Physical Review Letters*. **2014**, *113*, 086801.
- (32) Wang, Z.; McKeown Walker, S.; Tamai, A.; Wang Y.; Ristic Z.; Bruno F. Y.; de la Torre, A.; Riccò S.; Plumb N. C.; Shi M.; Hlawenka P.; Sánchez-Barriga, J.; Varykhalov, A.; Kim T. K.; Hoesch M.; King P. D. C.; Meevasana W.; Diebold, U.; Mesot, J.; Moritz, B. *et al.* Tailoring the Nature and Strength of Electron–Phonon Interactions in the SrTiO₃(001) 2D Electron Liquid. *Nature Materials*. **2016**, *15*, 835–839.
- (33) Laukhin, V.; Copie, O.; Rozenberg, M. J.; Weht, R.; Bouzehouane, K.; Reyren, N.; Jacquet, E.; Bibes, M.; Barthélémy, A.; Herranz, G. Electronic Subband Reconfiguration in ad0-Perovskite Induced by Strain-Driven Structural Transformations. *Physical Review Letters*. **2012**, *109*, 226601.
- (34) Herranz, G.; Singh, G.; Bergeal, N.; Jouan, A.; Lesueur, J.; Gázquez, J.; Varela, M.; Scigaj, M.; Dix, N.; Sánchez, F.; Fontcuberta, J. Engineering Two-Dimensional Superconductivity and Rashba Spin–Orbit Coupling in LaAlO₃/SrTiO₃ Quantum Wells by Selective Orbital Occupancy. *Nature Communications*. **2015**, *6*, 6028.
- (35) Straub, Th.; Claessen, R.; Steiner, P.; Hüfner, S.; Eyert, V.; Friemelt, K.; Bucher, E. Many-Body Definition of a Fermi Surface: Application to Angle-Resolved Photoemission. *Phys. Rev. B*. **1997**, *55*, 13473.
- (36) Salluzzo, M.; Cezar, J. C.; Brookes, N. B.; Bisogni, V.; De Luca, G. M.; Richter, C.; Thiel, S.; Mannhart, J.; Huijben, M.; Brinkman, A.; Rijnders, G.; Ghiringhelli, G. Orbital Reconstruction and the Two-Dimensional Electron Gas at the LaAlO₃/SrTiO₃ Interface. *Phys. Rev. Lett.* **2009**, *102*, 166804.
- (37) Zabaleta, J.; Borisov, V. S.; Wanke, R.; Jeschke, H. O.; Parks, S. C.; Baum, B.; Teker, A.; Harada, T.; Syassen, K.; Kopp, T.; Pavlenko, N.; Valentí, R.; Mannhart, J. Hydrostatic

Pressure Response of an Oxide-Based Two-Dimensional Electron System. *Physical Review B*. **2016**, *93*, 235117.

- (38) Krsnik, J.; Strocov, V. N.; Nagaosa, N.; Barisic, O. S.; Rukelj, Z.; Yakubeny, S. M.; Mishchenko, A. S. Manifestation of the Electron-Phonon Interaction Range in the Angle Resolved Photoemission Spectra. *Physical Review B* **2020**, *102*, 121108(R)
- (39) Joshua, A.; Pecker, S.; Ruhman, J.; Altman, E.; Ilani, S. A Universal Critical Density Underlying the Physics of Electrons at the LaAlO₃/SrTiO₃ Interface. *Nat. Commun.* **2012**, *3*, 1–7.
- (40) Gan, Y.; Christensen, D. V.; Zhang, Y.; Zhang, H.; Krishnan, D.; Zhong, Z.; Niu, W.; Carrad, D. J.; Norrman, K.; von Soosten, M.; Jespersen, T. S.; Shen, B.; Gauquelin, N.; Verbeeck, J.; Sun, J.; Pryds, N.; Chen, Y. Diluted Oxide Interfaces with Tunable Ground States. *Advanced Materials*. **2019**, *31*, 1805970.
- (41) Luttinger, J. M. Fermi Surface and Some Simple Equilibrium Properties of a System of Interacting Fermions. *Physical Review*. **1960**, *119*, 1153
- (42) Scopigno, N.; Bucheli, D.; Caprara, S.; Biscaras, J.; Bergeal, N.; Lesueur, J.; Grilli, M. Phase Separation from Electron Confinement at Oxide Interfaces. *Phys. Rev. Lett.* **2016**, *116*, 026804.
- (43) Dudy, L.; Sing, M.; Scheiderer, P.; Denlinger, J. D.; Schütz, P.; Gabel, J.; Buchwald, M.; Schlueter, C.; Lee, T.-L.; Claessen, R. *In Situ* Control of Separate Electronic Phases on SrTiO₃ Surfaces by Oxygen Dosing. *Advanced Materials*. **2016**, *28*, 7443–7449.
- (44) King, P. D. C.; McKeown Walker, S.; Tamai, A.; de la Torre, A.; Eknapakul, T.; Buaphet, P.; Mo, S.-K.; Meevasana, W.; Bahramy, M. S.; Baumberger, F. Quasiparticle Dynamics and Spin–Orbital Texture of the SrTiO₃ Two-Dimensional Electron Gas. *Nat. Commun.* **2014**, *5*, 3414
- (45) Biscaras, J.; Hurand, S.; Feuillet-Palma, C.; Rastogi, A.; Budhani, R. C.; Reyren, N.; Lesne, E.; Lesueur, J.; Bergeal, N. Limit of the Electrostatic Doping in Two-Dimensional Electron Gases of LaXO₃(X = Al, Ti)/SrTiO₃. *Scientific Reports* **2015**, *4*, 6788
- (46) Herranz, G.; Basletić, M.; Bibes, M.; Carrétéro, C.; Tafr, E.; Jacquet, E.; Bouzouane, K.; Deranlot, C.; Hamzić, A.; Broto, J.; Barthélémy, A.; Fert, A. High Mobility in LaAlO₃/SrTiO₃ Heterostructures: Origin, Dimensionality, and Perspectives. *Physical Review Letters*. **2007**, *98*, 216803.

- (47) Mishchenko, A. S.; Nagaosa, N.; Alvermann, A.; Fehske, H.; De Filippis, G.; Cataudella, V.; Sushkov, O. P. Localization-Delocalization Transition of a Polaron near an Impurity. *Physical Review B*. **2009**, *79*, 180301.
- (48) Pallecchi, I.; Telesio, F.; Li, D.; Fête, A.; Gariglio, S.; Triscone, J.-M.; Filippetti, A.; Delugas, P.; Fiorentini, V.; Marré, D. Giant Oscillating Thermopower at Oxide Interfaces. *Nat. Commun.* **2015**, *6*, 6678.
- (49) Shinozuka, Y.; Toyozawa, Y. Self-Trapping in Mixed Crystal – Clustering, Dimensionality, Percolation. *Journal of the Physical Society of Japan*. **1979**, *46*, 505–514.
- (50) Candia, A. de; de Candia, A.; De Filippis, G.; Cangemi, L. M.; Mishchenko, A. S.; Nagaosa, N.; Cataudella, V. Two-Channel Model for Optical Conductivity of High-Mobility Organic Crystals. *EPL (Europhysics Letters)*. **2019**, *125*, 47002.
- (51) Filippis, G. D.; De Filippis, G.; Cataudella, V.; Mishchenko, A. S.; Nagaosa, N.; Fierro, A.; de Candia, A. Crossover from Super- to Subdiffusive Motion and Memory Effects in Crystalline Organic Semiconductors. *Physical Review Letters*. **2015**, *114*, 086601.
- (52) Mishchenko, A. S.; Pollet, L.; Prokof'ev, N. V.; Kumar, A.; Maslov, D. L.; Nagaosa, N. Polaron Mobility in the “Beyond Quasiparticles” Regime. *Physical Review Letters*. **2019**, *123*, 076601.
- (53) Trier, F.; Christensen, D. V.; Pryds, N. Electron Mobility in Oxide Heterostructures. *Journal of Physics D: Applied Physics*. **2018**, *51*, 293002.
- (54) Boschker, H.; Richter, C.; Fillis-Tsirakis, E.; Schneider, C. W.; Mannhart, J. Electron-Phonon Coupling and the Superconducting Phase Diagram of the LaAlO₃–SrTiO₃ Interface. *Scientific Reports*. **2015**, *5*, 12309.
- (55) Strocov, V. N.; Wang, X.; Shi, M.; Kobayashi, M.; Krempasky, J.; Hess, C.; Schmitt, T.; Patthey, L. Soft-X-Ray ARPES Facility at the ADRESS Beamline of the SLS: Concepts, Technical Realisation and Scientific Applications. *J. Synchrotron Radiat.* **2014**, *21* (Pt 1), 32–44.
- (56) Strocov, V. N.; Schmitt, T.; Flechsig, U.; Schmidt, T.; Imhof, A.; Chen, Q.; Raabe, J.; Betemps, R.; Zimoch, D.; Krempasky, J.; Wang, X.; Grioni, M.; Piazzalunga, A.; Patthey, L. High-Resolution Soft X-Ray Beamline ADRESS at the Swiss Light Source for Resonant Inelastic X-Ray Scattering and Angle-Resolved Photoelectron Spectroscopies. *J. Synchrotron Radiat.* **2010**, *17*, 631–643.

Band-Order Anomaly at the γ -Al₂O₃/SrTiO₃ Interface Drives the Electron-Mobility Boost (Supporting Information)

Alla Chikina,¹ Dennis Valbjørn Christensen,² Vladislav Borisov,³ Marius-Adrian Husanu,^{1,4}
Yunzhong Chen,² Xiaoqiang Wang,¹ Thorsten Schmitt,¹ Milan Radovic,¹ Naoto Nagaosa,⁵ Andrey
S. Mishchenko,⁵ Roser Valentí,³ Nini Pryds² & Vladimir N. Strocov¹

¹*Swiss Light Source, Paul Scherrer Institute, 5232 Villigen-PSI, Switzerland*

²*Department of Energy Conversion and Storage, Technical University of Denmark, 2800 Kgs.
Lyngby, Denmark*

³*Institut für Theoretische Physik, Goethe-Universität Frankfurt am Main, 60438 Frankfurt am Main,
Max-von-Laue-Strasse 1, Germany*

⁴*National Institute of Materials Physics, Atomistilor 405A, 077125 Magurele, Romania*

⁵*RIKEN Center for Emergent Matter Science, 2-1 Hirosawa, Wako, Saitama 351-0198, Japan*

Ti *L*-edge resonant photoemission: 2DES vs IG states

The Ti *L*-edge resonant photoemission (ResPE) maps for our oxygen-deficient LAO/STO and low- n_s GAO/STO are presented in Fig. S1. The maps were acquired at a saturation dose of X-ray irradiation. The ARPES intensity was integrated within $\pm k_F^{yz}$. The maps show the valence band (marked VB), IG states (IG) and mobile 2DES states (2DES) whose spectral response dramatically varies as a function of excitation energy. The VB signal, resonating at the $\text{Ti}^{4+} t_{2g}$ and e_g peaks of X-ray absorption, represents the oxygen-derived states hybridized with Ti in the STO bulk. The VO-derived IG states resonate at the $\text{Ti}^{3+} e_g$ absorption peak, and the 2DES states are delayed from the $\text{Ti}^{4+} t_{2g}$ peaks. This difference in excitation energies reflects the $\text{Ti}^{3+} e_g$ character of the former vs $\text{Ti}^{4+} t_{2g}$ character of the latter, for the full analysis see A. Chikina *et al*, ACS Nano **12** (2018) 7927.

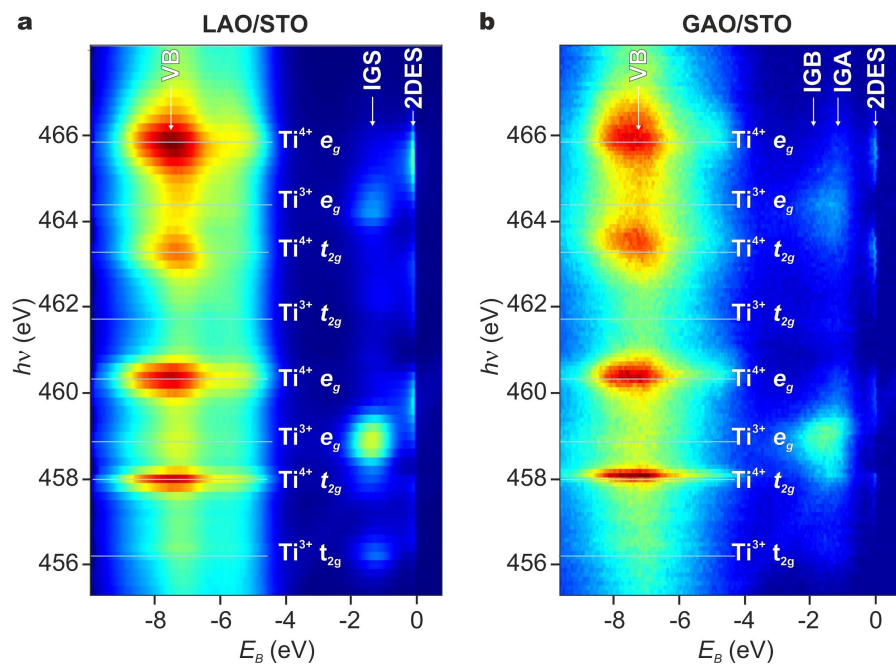


Fig. S1. ResPE maps for LAO/STO (a) and low- n_s GAO/STO (b) samples. The latter shows two different IG states.

Remarkably, the ResPE map for GAO/STO shows two IG states, one at $E_B \sim 1.2$ eV (marked IGA) and another at -2.1 eV (marked IGB) (P. Schütz *et al*, Phys. Rev. B **96** (2017) 161409). The IGA spectral weight scales up under X-ray irradiation, and can be quenched by irradiation in oxygen atmosphere (A. Chikina *et al*, ACS Nano **12** (2018) 7927; V. N. Strocov *et al*, Phys. Rev. Materials

3 (2019) 106001). The IGB, in contrast, is immune to the irradiation and oxygen atmosphere. While the IGA state is characteristic of the V_{O} s created by X-ray irradiation at bare STO surfaces and LAO/STO interfaces, the IGB one can be associated, tentatively, with fixed V_{O} s created during the sample growth in the top STO layer interfaced with GAO. The experimental ResPE map shows different excitation-energy dependence of the two states, identifying their different nature. Crystal-field calculations supporting this scenario of the formation of the IGA and IGB states were discussed in the Supplemental Materials of the above paper by P. Schütz *et al.*

Effective-mass analysis

Experimental values of the effective mass m^*/m_0 (m_0 is the free-electron mass) for the d_{xz} and d_{yz} bands are compiled in the table below. They were calculated from the experimental values of k_F indicated in Fig. 2 (determined from extremes of the gradient dI/dk_x of the MDCs at E_F) and energies E_{bot} of the d_{xz}/d_{yz} band bottom. The uncertainty of k_F and E_{bot} has been determined from the scatter of their measurements through the experimental series.

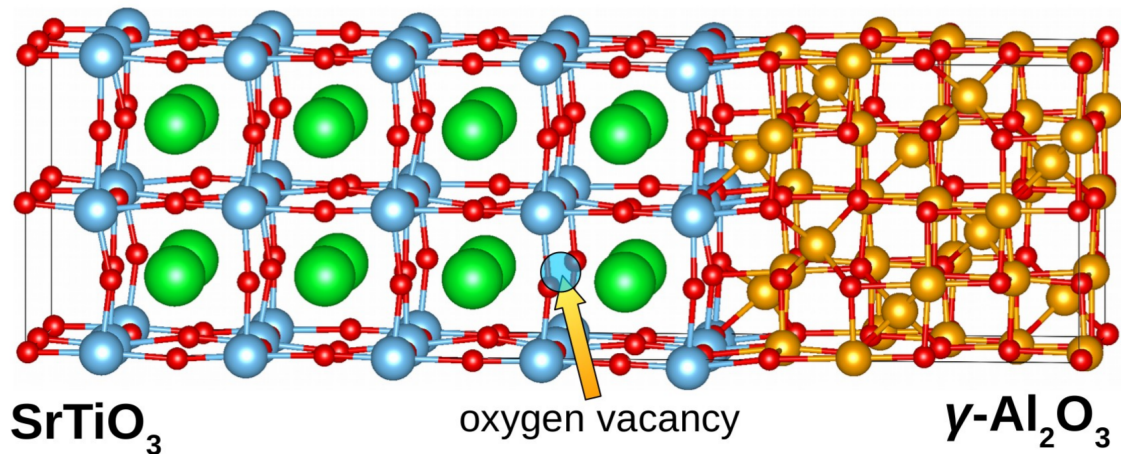
m^*/m_0	LAO/STO	low- n_s GAO/STO	high- n_s GAO/STO
d_{xz}	0.72 ± 0.32	0.32 ± 0.22	0.40 ± 0.23
d_{yz}	11.5 ± 2.5	6.0 ± 1.2	9.8 ± 1.3

DFT calculations

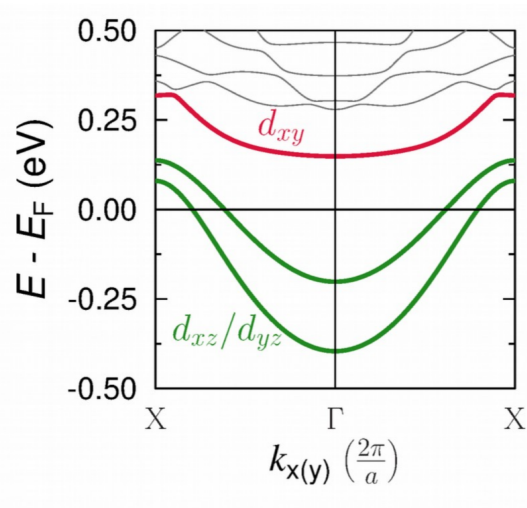
In order to get more insight into the nature of electronic states at the GAO/STO interface, we performed DFT simulations for the supercell structures shown in Fig. S2 (a) that include an appropriate lattice matching between the two oxides and allow for modeling realistic concentrations of V_O s. Since the 2DES here is dominated by the Ti 3d electrons, the electronic correlations were taken into account using the GGA+ U corrections for these states (S. L. Dudarev *et al*, Phys. Rev. B **57** (1998) 1505). The GAO/STO interface was simulated by the superlattice (P. Schütz *et al*, Phys. Rev. B **96** (2017) 161409) where 4.5 u.c. of [001]-oriented STO were attached to five tetragonal and five octahedral Al layers of the Al_3O_4 spinel structure. One unit cell of GAO contains four layers of each type. We chose an in-plane (2×2) superlattice of the standard perovskite unit cell of STO to match the oxygen sublattices of the two materials. In order to take into account the defect-spinel structure of GAO where Al vacancies are distributed over the tetragonal and octahedral Al sites, we simulated a random distribution of cationic vacancies through the virtual crystal approximation (VCA) (L. Bellaiche and D. Vanderbilt, Phys. Rev. B **61** (2000) 7877) where the charge of each Al cation is shifted by 1/3 towards Mg leading to a nuclear charge $Z=12+2/3$. We consider a V_O in the sublayer, Fig, S2 (a). In this case, the electrons donated by the V_O are not fully localized.

The results of our DFT calculations provide important insights into the electronic structure of the spinel-perovskite GAO/STO interface. First of all, for most V_O configurations the interface is conductive, and the \mathbf{k} -resolved band structure in Fig. S2 (c) projected on the Ti sites indicates an inverted band ordering in GAO/STO with the d_{xz}/d_{yz} orbitals lying well below d_{xy} . This is opposite to the situation typically observed in LAO/STO, Fig. S2 (d), and other oxide heterostructures (A. Chikina *et al*, ACS Nano **12** (2018) 7927). The hybridization between the d_{xz} and d_{yz} bands in GAO/STO, symmetry-forbidden in LAO/STO, results from the non-symmetric position of the V_O in the supercell. The overestimate of \mathbf{k}_F is an artifact of the limited supercell size in our calculations.

a) GAO/STO interface structure



b) GAO/STO band structure



c) LAO/STO band structure

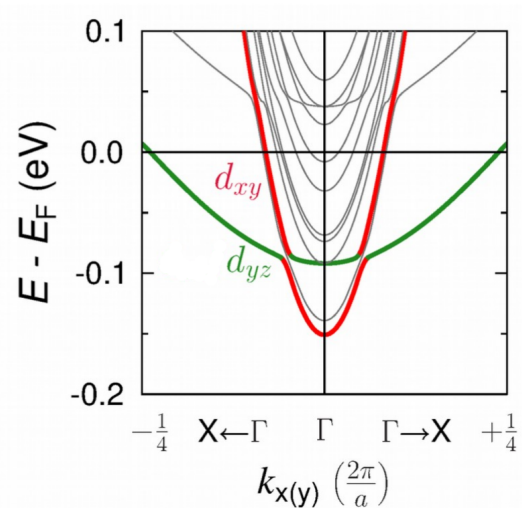


Fig. S2. Crystal and electronic structure of the oxygen-deficient GAO/STO interface. (a) Sketch of the GAO/STO supercell simulating the interface with a single V_O (the arrow); (b,c) Calculated band structures for the oxygen-deficient GAO/STO and defect-free LAO/STO interfaces (the latter is adapted from J. Zabaleta *et al*, Phys. Rev. B **93** (2016) 235117) along the $X\Gamma X$ direction. The dominant orbital character is encoded by color: red (d_{xy}) and green (d_{xz}/d_{yz}).

Experimental Fermi surface of GAO/STO

Another interesting peculiarity of GAO/STO seen in Fig. S3 (a), absent for LAO/STO, is notable streaks of the Fermi intensity stretching along the ΓX directions across the BZs. This peculiarity should manifest a lateral disorder in GAO/STO along the (100) crystallographic directions. Such a disorder can manifest formation of a rectangular-pattern, as schematized in Fig. S3 (c). The origin of this disorder is not yet clear, but potential candidates could be (1) linear clusters of the interfacial V_{O_s} in GAO/STO, with their linear arrangement being slightly energetically preferred (F. Cordero, Phys. Rev. B **76** (2007) 172106; D. D. Cuong *et al*, Phys. Rev. Lett. **98** (2007) 115503), or (2) rectangular domains, whose dimensions are comparable with the ARPES coherence length, although our scanning-SQUID measurements on similarly prepared samples have only found micron-size domains (D. Christensen *et al*, Phys. Rev. Applied **9** (2018) 054004) typical of the STO-based systems (Frenkel *et al*, Nat. Mater. **16** (2017) 1203). We note that similar streaks in the FS map were observed at bare BaTiO₃ surfaces and interpreted in terms of the Wannier-Stark electron localization in a strong electric field between the ferroelectric domains of BaTiO₃ (S. Muff *et al*, Phys. Rev. B **98** (2018) 045132). Such a strong electric field is however absent at the GAO/STO interface.

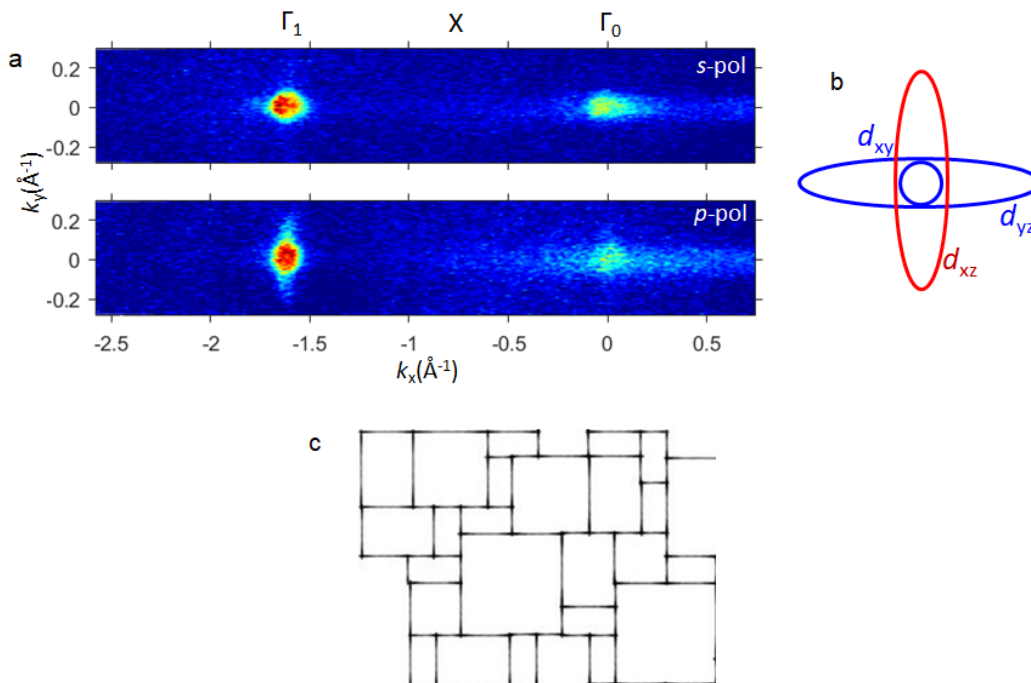


Fig. S3. (a) FS map of GAO/STO acquired at the Ti L_3 -edge ($h\nu=460.2$ eV). s- and p-polarization of incident X-rays selects electron states of different symmetry as schematized in (b); (c) A random-rectangle disorder pattern explaining the Fermi-intensity streaks along the ΓX direction.